Editors' Suggestion

Behavior of Sm in the boron cage of Sm-doped RB_6 (R =Yb, La) observed by multiple-wavelength neutron holography

Shoichi Uechi,[1] Kenji Ohoyama,[1,*] Yohei Fukumoto,[1,†] Yuki Kanazawa,[1] Naohisa Happo,[2] Masahide Harada,[3] Yasuhiro Inamura,[3] Kenichi Oikawa,[3] Wataru Matsuhra,[4] Fumitoshi Iga,[4] Artoni Kevin R. Ang,[5] and Kouichi Hayashi[5,6]

[1]*Graduate School of Science and Engineering, Ibaraki University, Tokai 319-1106, Japan*

[2]*Graduate School of Information Sciences, Hiroshima City University, Hiroshima 731-3194, Japan*

[3]*Materials and Life Science Division, J-PARC Center, Tokai 319-1195, Japan*

[4]*Graduate School of Science and Engineering, Ibaraki University, Mito 310-8512, Japan*

[5]*Department of Physical Science and Engineering, Nagoya Institute of Technology, Nagoya 466-8555, Japan*

[6]*Frontier Research Institute for Materials Research, Nagoya Institute of Technology, Nagoya 466-8555, Japan*

(Received 6 April 2020; accepted 4 August 2020; published 24 August 2020)

We have succeeded in visualizing the local atomic structures around Sm in RB_6 (R = Yb, La), in which a rare-earth atom is located in the boron cage, using the newly developed technique for local structure investigations, multiple-wavelength neutron holography in a pulsed neutron facility. From the local atomic structures, we were able to clarify the behavior of Sm in the boron cage. Doped Sm in YbB_6 fluctuates within the boron cage with a mean displacement of 0.25(4) Å, while that of Sm in LaB_6 is approximately 0.15 Å. The Sm doping causes the fluctuation of the first-nearest-neighbor B with a mean displacement of 0.28 Å, while its effect on La, Yb, and the rest of the boron atoms is negligible. These are the first observations of the local behavior of doped rare-earth atoms and B in rare-earth borides with boron cages.

DOI: 10.1103/PhysRevB.102.054104

I. INTRODUCTION

Hexaborides have attracted significant scientific interest because of their unique electric, magnetic, and physical properties, such as their high electrical conductivity, competition between their magnetic and multipolar orderings, rattling motions, and so on [1,2]. Many of these exotic properties stem from their crystal structures, which contain a network of strongly bonded boron cages. The crystal structure of rare-earth hexaborides RB_6 (R = rare earth) consists of a rare-earth atom surrounded by a boron cage, as is illustrated in Fig. 1. In these RB_6 systems, anomalous phonon softening was observed by inelastic x-ray scattering in heavy R hexaborides, such as GdB_6, TbB_6, and DyB_6 [3–5]. The dispersion of the longitudinal phonon of the R motions of the RB_6 (R = Gd, Tb, Dy) propagating along the [100] direction exhibits maxima and bends downward toward the Brillouin zone boundary. The phonon energy at the zone boundary decreases by 10%–30% from room temperature to about 20 K, which is due to electron-phonon coupling [5]. This softening induces the instability of the RB_6 lattice with heavier rare-earth atoms. The softening becomes stronger systematically in the order of R = Gd, Tb, and Dy, in other words, with decreasing ionic radius [5,6]. The softening was also observed by Raman scattering, where the energy and intensity of the R motions can be scaled by the free space in the boron cage $\delta r = a - 2r_R$, where a and r_R are the lattice constant and ionic radius of the R ions, respectively [7–9]. Thus, the free space for the R motion in the boron cage must be a significant factor.

On the other hand, the dispersion curve of phonons in YbB_6 is significantly different from those of RB_6 (R = Gd, Tb, Dy); the dispersion relation along the [100] direction is a monotonous increase toward the zone boundary [6]. The difference of these dispersion curves must be due to the divalency of Yb in YbB_6, while R in RB_6 (R = Gd, Tb, Dy) is trivalent. The coupling between rare-earth ions in $R^{2+}B_6$ is thought to be stronger than that in $R^{3+}B_6$ according to first-principles calculations [9]. To consider R^{3+} motions in the boron cage in YbB_6, Sm-doped YbB_6 must be a good target because, when a few percent of Sm are doped, Sm is trivalent in $Yb^{2+}B_6$ [10,11].

On the other hand, in Sm-doped LaB_6, Sm is close to divalent [10]. The difference in the ionic radii of Sm^{3+} and Sm^{2+} is ∼0.2 Å according to the effective ionic radius for eight-coordination reported by Shannon [12], which is 20 times larger than the difference of the lattice constants of YbB_6 and LaB_6 [13,14]. This means that the free space of Sm motions in YbB_6 is much larger than that in LaB_6. Therefore, the observation and comparison of the behavior of Sm dopants in the boron cages of YbB_6 and LaB_6 should provide information on the R motions in the RB_6 system

Atomic resolution holography is a novel probe which can visualize structures and the behavior of atoms around atoms of a target element (dopants) with atomic resolution [15–19]. The key advantages of atomic resolution holography in comparison with other techniques, such as conventional diffraction techniques, pair distribution function (PDF) techniques,

*kenji.ohoyama.vs@vc.ibaraki.ac.jp

†Present address: Foundation for Promotion of Material Science and Technology of Japan, Kitami 1-18-6, Tokyo 157,0067, Japan.

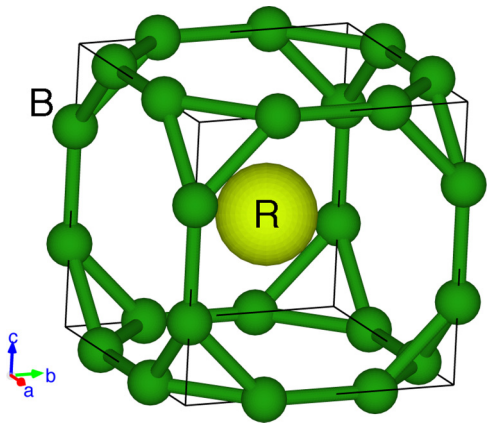

FIG. 1. Unit cell of RB_6 (R = rare earth). Space group is $Pm\bar{3}m$ (No. 221). The lattice constant is $a = 4.16$ Å for LaB_6.

and x-ray absorption fine structure (XAFS), are as follows: (1) holography is an element selective technique, meaning that only the signals from a particular element are observed, (2) three-dimensional (3D) atomic structures around dopants with atomic resolution can be directly visualized without prior models, and (3) the observable range is ∼20 Å from the dopants, which is much larger than that of XAFS, and the typical lattice constants of inorganic materials. Based on these advantages, x-ray fluorescence holography (XFH) and photoelectron holography (PEH) are already being actively used in investigating novel functional materials, such as dilute magnetic semiconductors, relaxor ferroelectric materials, topological insulators, and so on [20–28]. For this study, however, the target elements are rare earths and boron; thus, x rays and electrons are not effective because the sensitivity to boron in rare-earth compounds is insufficient. Thus, atomic resolution holography with neutrons is needed for this study because of its higher sensitivity to light elements.

Several different approaches to neutron-based holography have been proposed and demonstrated. Neutron holography using a Fresnel zone plate encoding by Beynon and Pink [29] and neutron holography with a neutron interferometer by Sarenac *et al.* [30] were successfully demonstrated by recording the hologram from macroscopic objects and reconstructing the image. On the other hand, atomic resolution neutron holography, which aims at visualizing the local atomic structures around atoms of a selected element, was first proposed by Cser *et al.* [31] and demonstrated by Sur *et al.* [32], and several experiments of atomic resolution neutron holography have already been reported since then [33–38]. These previous neutron holography experiments had been carried out at reactor facilities using neutrons with only a single wavelength because of the limited beam times. However, to enhance the accuracy of the visualization of atomic images obtained by holography, multiwavelength experiments are indispensable to minimize artifact images [19,39]; 5–10 wavelengths are used to suppress artifacts in a typical XFH experiment. Therefore, it will be difficult to obtain accurate atomic images by single-wavelength neutron holography, which will inevitably include many artifacts.

To significantly improve the accuracy of the atomic images, the authors have developed a technique named "multiple-wavelength neutron holography" (MNH) using white neutrons in a pulsed neutron facility [39,40], and succeeded in visualizing the three-dimensional (3D) local atomic structure around Eu in 1 % Eu-doped CaF_2, which is a typical scintillator crystal [40]. The measurements clarified that Eu^{3+} is located at Ca^{2+} positions, while there exist excess F^- ions around doped Eu^{3+} to maintain electrical neutrality. Therefore, MNH is a strong probe for local structure investigations of light elements, that is, to investigate the effects of Sm doping on the boron cage in Sm-doped RB_6. In this paper, we show the difference in the behavior of Sm in the boron cage in RB_6 (R = Yb and La), and the effects of this doping on the boron cages using MNH in a pulsed neutron facility.

II. EXPERIMENT

A. Experimental conditions

The MNH experiments were performed at the Beam line 10 (BL10) of the Materials and Life Science Experimental Facility (MLF) in Japan Proton Accelerator Research Complex (J-PARC), in Tokai, Japan [41,42]. The details of the MNH experiment in J-PARC are already reported elsewhere [39,40]. The essential point of MNH is that the intensity of prompt γ rays generated from the dopants provides direct information about the local atomic arrangement around the dopants because the γ-ray intensity corresponds to the interference of neutron waves in the sample. Since the dopants play a role of neutron detectors in the samples, this kind of technique is sometimes called *internal detector method.* In MNH, the atomic images around the dopants can be reconstructed from an intensity map of the γ rays as a function of the incident beam direction, which is called a hologram. Since the intensity of the prompt γ rays from an element is roughly proportional to the neutron absorption cross section σ_a of the element [39,43], suitable dopants for MNH are elements with larger σ_a, such as ^{10}B, Cd, Sm, and so on.

For this work, 2% Sm-doped RB_6 (R = Yb, La) single crystals were grown by the floating zone method using an image furnace with four xenon lamps [44]. The σ_a of Sm is 5922×10^{-24} cm^2 at $E = 25.3$ meV, while the σ_a of La and Yb are 8.97 and 34.8×10^{-24} cm^2 at $E = 25.3$ meV, respectively [45]. For the preparation, ^{11}B with a purity of 99.6% was used because natural B is a strong neutron absorber with $\sigma_a = 767 \times 10^{-24}$ cm^2 at $E = 25.3$ meV, that is, it generates γ rays as a strong background, while γ rays from ^{11}B, whose σ_a is 0.0055×10^{-24} cm^2 at $E = 25.3$ meV, can be negligible [45]. The expected intensity of prompt γ rays from Sm is reported to be approximately 3000 and 500 times stronger than those from La and Yb atom [43], thus, γ rays from 2% Sm-doped RB_6 (R = Yb, La) samples are mainly attributed to the Sm dopants. This means that the γ rays measured from the sample contains mostly local structure information around the Sm atoms.

A typical layout of the MNH instrument used in J-PARC is shown in Fig. 2. The γ rays from the samples were detected using a $Bi_4Ge_3O_{12}$ (BGO) γ-ray detector with a diameter of 6 cm. The BGO detector was covered by Pb blocks to reduce γ-ray background. The sample is rotated by a dual axes ϕ-ω goniometer set on the experimental table of BL10. The ω axis

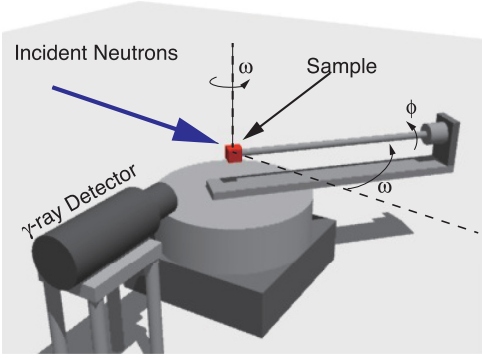

FIG. 2. Alignments of instruments of multiple-wavelength neutron holography (MNH) measurements in J-PARC.

is vertical, and ϕ axis is horizontal. The angle ω is defined as the angle between the direct beam and the ϕ axis. The flight pass from the neutron source to the sample position was 14.0 m, and the typical distance between the sample and the detector was 170 mm. Neutrons in the wavelength range of 0.38 Å–11.3 Å can be used for the experiments with a repetition rate of 25 Hz of J-PARC.

The experimental conditions for the Sm-doped RB_6 (R = Yb, La) samples were almost the same. The single-crystal samples were fixed at the tip of the horizontal aluminum rod on the ϕ goniometer. The samples were cylindrical with a diameter of 6 mm and length of 20 mm. The [001] axis of the sample was set approximately parallel to the ϕ axes. The directions of crystal axes were accurately determined by neutron Bragg reflections from the samples with an accuracy within 0.5°. The neutron beam size at the sample position was 30 mm× 30 mm, meaning that the samples were within the beam spot completely. The maximum angular divergence of the incident neutron beam was ±0.22° and ±0.25° in the horizontal and vertical directions, respectively.

The wavelength range of the incident beam used for the experiments was at most 0.38 Å–5.2 Å, which were divided into 130 channels to obtain multiple-wavelength holograms. The angular ranges were $10° \leqslant \omega \leqslant 170°$, and $0° \leqslant \phi \leqslant 360°$, where for each ω step ($\Delta\omega = 1°$) the sample is scanned along ϕ ($\Delta\phi = 0.45°$) at a speed of 0.45°/s. The γ-ray intensities were recorded by the event recording data acquisition system of J-PARC to connect angles of ϕ-ω and intensity, which results in holograms [46]. Typical scan time was approximately 20 h. Consequently, a two-dimensional intensity map (hologram) with 161 × 800 pixels can be obtained for each wavelength. To reduce the effects of the fluctuation of the beam flux in J-PARC, the holograms are normalized with an intensity map recorded in the 7.06 Å–11.3 Å range, where holographic signals are not expected [40]. For Sm-doped RB_6, the measurements were repeated for four times, and the four data sets were summed up to enhance intensity. Since the background intensity variation and absorption effect during one ϕ scan was almost constant, these effects were estimated using a cubic polynomial function, and were subtracted from each ϕ-scan data. The statistics of holograms can be enhanced using symmetry operations at the R position in the crystal structure of RB_6 (space group: $Pm\bar{3}m$).

B. Estimation of resolution

To discuss the reconstructed atomic images quantitatively, we estimated the experimental resolution of MNH using a nondoped Si single crystal as a standard sample under the same technique and conditions as the experiments on Sm-doped RB_6. In this measurement, Si itself plays a role of internal detectors. Even though γ rays generated from a Si atom, whose σ_a is 0.171×10^{-24} cm^2, is much weaker than that from Sm or ^{10}B, one can obtain holographic signals from Si itself because of a large number of Si atoms in a sample and higher sensitivity of MNH.

Figures 3(a) and 3(b) show the reconstructed atomic images in the (001) plane, in which the yellow part is the background and the red parts are the signals, and the profiles of the atomic images of the first-, second-, and third-nearest-neighbor (NN) Si taken along the radial direction, respectively. To compare the widths, the intensity is normalized by the peak intensity. By profile fitting using a Gaussian function of $\exp[-(r - r_0)^2/2\sigma_{\rm NH}^2]$+const, where $\sigma_{\rm NH}$ and r_0 are the widths and positions of the peaks, respectively, the $\sigma_{\rm NH}$ are obtained as shown in Fig. 3(c). Assuming that $\sigma_{\rm NH}$ is constant because no systematic dependence on distance was observed, $\sigma_{\rm NH}$ of the nondoped Si can be determined as the average value of $\sigma_{\rm NH}$ in Fig. 3(c), 0.23(4) Å. The error is defined as the standard deviation of the average.

The $\sigma_{\rm NH}$ of the atomic images from nondoped Si, in which the distortion of the lattice can be neglected, consists of two components $\sigma_{\rm NH}^2 = \sigma_{\rm Res}^2 + 2\langle u_{\rm Si}^2\rangle$, when Gaussian convolution of each component is assumed. In the calculation, $\langle u_{\rm Si}^2\rangle$ is the mean-square displacement by thermal vibrations of Si, where u is displacement from the ideal position of Si in the lattice, and $\sigma_{\rm Res}$ is instrumental resolution of MNH. Since $\langle u_{\rm Si}^2\rangle$ can be determined as 0.0057(3) Å [47] using the isotropic atomic displacement factor $B = 8\pi^2\langle u^2\rangle$, obtained from diffraction experiments, which is 10 times smaller than $\sigma_{\rm NH}^2$. Consequently, $\sigma_{\rm Res}$ of MNH is estimated as $\sigma_{\rm Res} = 0.20(5)$ Å.

III. RESULTS AND DISCUSSION

A. Atomic images

Examples of the experimental holograms with $\lambda = 2.37$ Å recorded from LaB_6 and YbB_6 are shown in Figs. 4(a) and 4(b). The radial and angular directions correspond to ω and ϕ, respectively. The vertical and horizontal arrows indicate the [100] and [010] crystal axes determined from the neutron Bragg reflections from the samples. We successfully observed geometrical patterns with an approximately 1% undulation, which originate from neutron standing waves due to the interference around Sm within the samples. For comparison, the hologram pattern was simulated and shown in Fig. 4(c) using a cluster model of LaB_6 with a radius of 50 Å, which is larger than the typical observable range of holography.

Comparing the holograms, the fundamental structures of the experimental holograms are basically the same as those of the simulation, for instance, the leaf-shaped pattern in the dashed oval lines, indicating that local atomic structures around Sm in RB_6 are successfully observed by MNH. The reason why the color in Figs. 4(b) and 4(c) is reversed may be due to the contamination of holograms from ^{10}B. Since

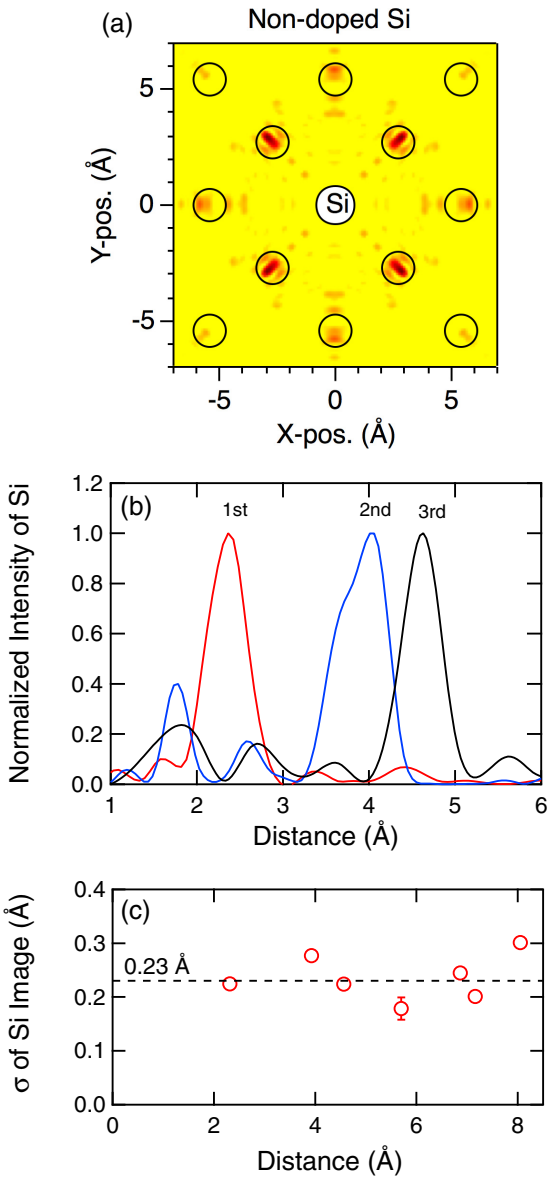

FIG. 3. (a) Reconstructed atomic images $|U(\vec{R})|$ of the (001) plane around a Si. The yellow part is the background, and the red parts are the signals. The centers of the open circles are the expected positions of Si. (b) Profiles of the atomic images of the first, second and third NN Si atom from a central Si atom along the radial direction. (c) The width σ_{NH} of each profile determined by Gaussian fitting.

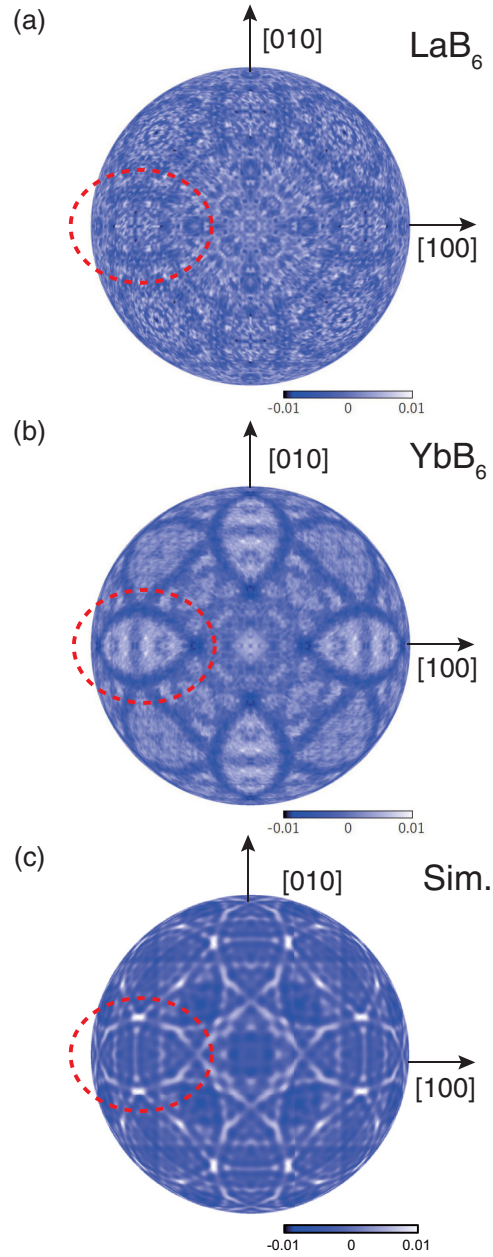

FIG. 4. Examples of full holograms recorded at $\lambda = 2.37$ Å from (a) 2% Sm-doped LaB_6, (b) 2% Sm-doped YbB_6, and (c) simulated hologram of LaB_6. The directions of crystal axes are also shown. The dashed oval lines indicate features observed in all holograms.

enrichment of ^{11}B for sample preparation was not perfect, the samples included small amount of ^{10}B, which generate γ ray by neutron absorption, in other words, it generates holograms, which mainly consist of negative (blue) lines. On the other hand, the patterns from LaB_6 [Fig. 4(a)] are not obvious. Possible reasons may be the difference of scattering lengths b of La ($b = 8.24\times10^{-15}$ m) and Yb ($b = 12.43 \times 10^{-15}$ m), and the difference of the beam flux of MLF; the neutron beam flux during the measurements of LaB_6 was a half of that of YbB_6. Furthermore, the difference in the vibration of Sm atoms, which will be discussed later, may also be a factor.

From the 61 experimental holograms recorded in 0.63 Å–2.57 Å range, the atomic images in the (001) plane were reconstructed using Barton's method as shown in Fig. 5 [35,48,49]. This plane contains the Sm atoms of the Sm-doped RB_6 (R = Yb, La). In Figs. 5, 6, and 11, the yellow part is the background, and the red parts are the signals. In the reconstructions in Fig. 5, the atomic images can be observed in the circles whose centers are the expected positions of R in RB_6, meaning that the local structures of R around Sm are successfully visualized by MNH. It should be emphasized that Fig. 5 is not an averaged crystal structure obtained by

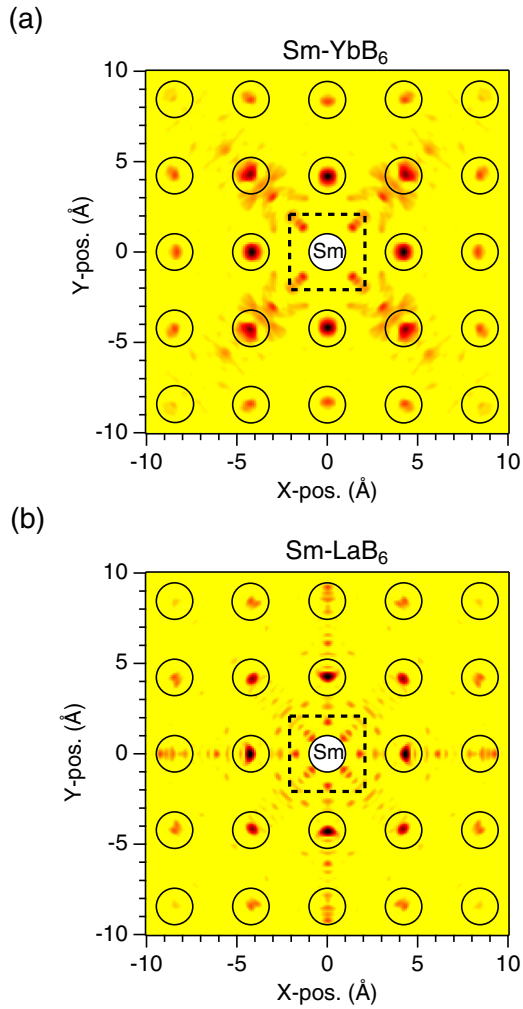

FIG. 5. Reconstructed atomic images $|U(\vec{R})|$ of the (001) plane around doped Sm in 2% Sm-doped YbB_6 (a), and LaB_6 (b). The dashed squares indicate a unit cell in the plane. The expected positions of R in nondoped RB_6 are the centers of the open circles.

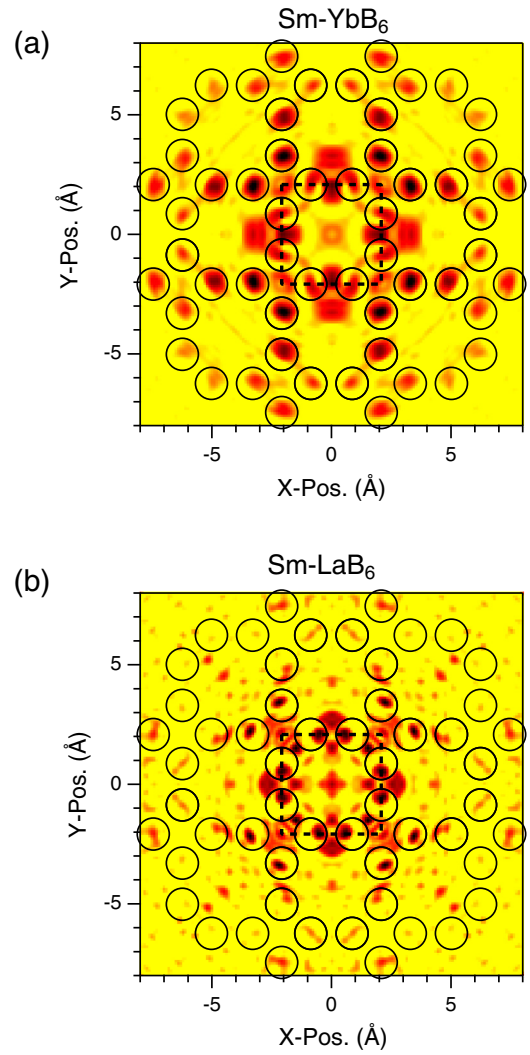

FIG. 6. Reconstructed atomic images $|U(\vec{R})|$ of the (001) boron plane located at 2.08 Å ($= 1/2a$) above the Sm atom in (a) Sm-doped YbB_6 and in (b) Sm-doped LaB_6. The central squares indicate the unit cells in the planes. The expected positions of B are the centers of the open circles.

the conventional diffraction technique, but is the local atomic structure which exists *only* around Sm dopants.

Figure 6 is the reconstruction of the (001) plane located approximately 2.08 Å ($= 1/2a$) above Sm, which only contains B atoms. Atomic images can be visualized within the circles as well. Compared with Fig. 5, there are more visible signals outside these circles, which are thought to be artifacts because these signals are too distant from the centers of the circles, which are the expected positions of B. Since the boron-cage structure is more complicated, the intensity of B atomic images in the circles becomes relatively weaker, which becomes almost comparable with the artifacts; moreover, the intensity of B images is suppressed by fluctuations, as will be discussed later.

Both Figs. 5 and 6 demonstrate that MNH is an effective technique to directly observe the local structures of light elements, such as B, H, Li, around dopants. This is important because such light elements play important roles in functional materials, such as Li batteries, or hydrogen storage materials and so on, as well as rare-earth borides.

B. Behavior of Sm in the boron cage

Here, we discuss the behavior of the Sm dopants in the boron cage. Figure 7(a) shows the profiles of the atomic images of the first-NN rare-earth atoms along the radial direction from the Sm dopants. From the peak fitting using the Gaussian function, $\exp[-(r-r_0)^2/2\sigma_{\rm NH}^2]$+const, the $\sigma_{\rm NH}$ of the profiles of the first NN R is determined as 0.32(1) Å for YbB_6, and 0.17(4) Å for LaB_6. As a function of distance from the Sm atoms [Fig. 7(b)], the $\sigma_{\rm NH}$ of Yb (blue) is almost constant, while those of La (red) slightly increases until it becomes almost the same with those of Yb above above 9 Å. This implies that the broadening of La is relatively reduced in the vicinity of Sm atoms.

Comparing with the $\sigma_{\rm Res}$ determined from the Si profiles, the $\sigma_{\rm NH}$ of the first-NN La for Sm-doped LaB_6 shows no significant difference from $\sigma_{\rm Res}$, while that for Sm-doped YbB_6 is 1.6 times larger than $\sigma_{\rm Res}$. Using $\sigma_{\rm Res} = 0.20(5)$ Å,

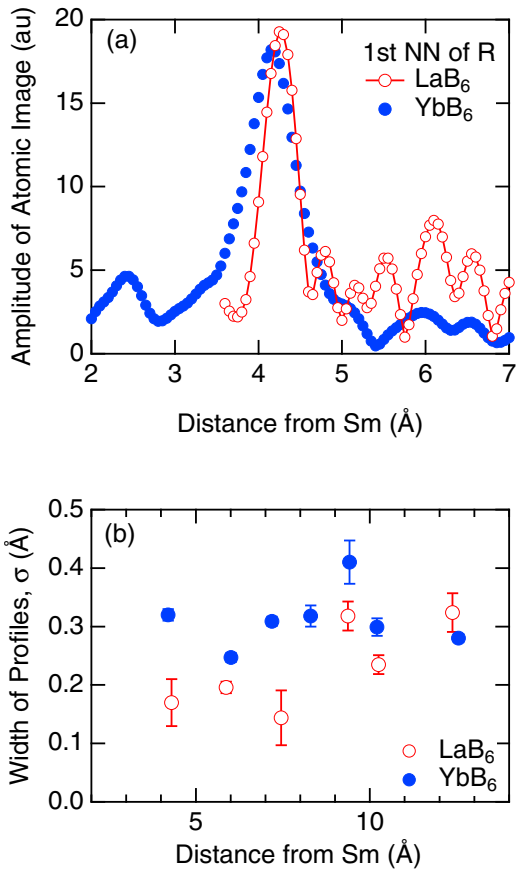

FIG. 7. (a) Profile of atomic images of the first-NN rare-earth atoms (La, Yb) along the radial direction from Sm. (b) Width of the profiles σ_{NH} as a function of the distance from Sm.

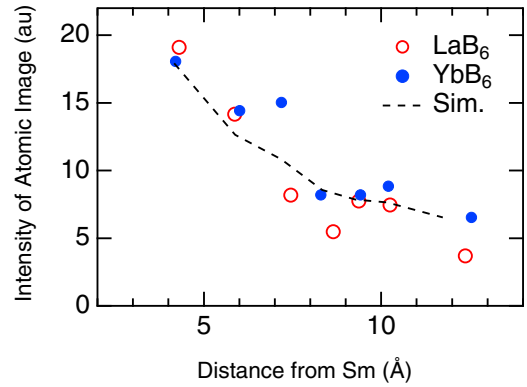

FIG. 8. Intensity of atomic images of La (open circles) and Yb (closed circles) of Sm-doped LaB_6 and YbB_6 as a function of the distance from Sm. The intensity is defined as the value of the peak top of each atomic image. The dashed line is the simulation using a model without distortion, which is scaled by the first-NN Yb of Sm-doped YbB_6.

the intrinsic width σ_R of the profiles of the first-NN Yb in Sm-doped YbB_6 was estimated as $\sigma_R = 0.25(4)$ Å, assuming the Gaussian convolution $\sigma_{NH}^2 = \sigma_{Res}^2 + \sigma_R^2$. The σ_R of the first NN in Sm-doped LaB_6 is discussed later based on the suppression of the intensity.

The intrinsic width of the profiles σ_R consists of the fluctuations of the positions of both Sm and R(Yb, La). However, the fluctuations of Sm and R cannot be distinguished from the profiles. Thus, to estimate the fluctuation of R(Yb, La), we analyzed the intensity of the atomic images. In the distance dependence of the peak intensity of the atomic images of La and Yb in Fig. 8, the intensity decreases with increasing distance; this is similar with the typical feature of atomic images obtained by XFH [18,19]. The distance dependence of the atomic images of Yb and La is nearly the same. To discuss the intensity of R in Fig. 8, we compared the observed intensity with the peak intensities from simulations, using a cluster model of nondistorted RB_6 structure with a cluster size of 20 Å, which is larger than the observable region in MNH [50,51]. The simulated intensity (dashed line) is normalized with the first-NN Yb of Sm-doped YbB_6. As discussed later quantitatively, when atoms around the dopant fluctuates, the intensity will be suppressed [52,53]. However, the agreement between the observed and calculated intensities are satisfactory. In XFH, it is known that the distance dependence of the intensity of the atomic images is not affected by the fluctuations of the dopant atoms [53]. Thus, since the fluctuations of R by Sm doping at around 12 Å are expected to be negligible, the agreement means that the fluctuations of R can be negligible even for the first-NN R, or R atoms in the vicinity of the Sm dopants are fluctuating with the same phase with the Sm dopants, as discussed later. Therefore, the origin of the intrinsic width of the profile in Fig. 7 is due to the fluctuation of the Sm dopant atoms in the boron cage with $\sigma_{Sm} = 0.25(4)$ Å.

On the other hand, since the intensities of the atomic images are proportional to the scattering length b of La and Yb [39,40], which are 8.24×10^{-15} m and 12.43×10^{-15} m, respectively [45], the intensity of Yb must be 1.5 times of those of La. Thus, the roughly same intensity of La and Yb in Fig. 8 means that the intensity of Yb is suppressed to 70% of the expected value from b. It is highly probable that this suppression is due to the fluctuation of Sm in the boron cage because of the following quantitative analysis. The fluctuation is represented by using the Box-Muller method with an isotropic Gaussian distribution $G(r) = \exp[-r^2/2\sigma^2]$, where r and σ are the distance from the ideal position of the atom and the isotropic mean-square displacement, respectively. In the calculations, La and Yb are fixed at the ideal positions without any fluctuations. The intensity of the first-NN R is shown with open red circles in Fig. 9 as a function of the mean displacement of Sm, σ_{Sm}. The intensity of the atomic images of R (Yb or La) monotonically decreases with increasing σ_{Sm}; this is the typical feature by the effect of atomic fluctuations observed by XFH [52,53]. From the calculation, the intensity of the first-NN Yb at $\sigma_{Sm} = 0.25(4)$ Å, which was estimated from the profiles in Fig. 7, becomes 27(6)% of that at $\sigma_{Sm} = 0$ Å. On the other hand, if the Sm atoms in LaB_6 also fluctuate at $\sigma_{Sm} = 0.15$ Å, the intensity of the La atomic images becomes 50% of that at $\sigma_{Sm} = 0$ Å. Consequently, the same intensity of Yb and La atomic images can be expected by the suppression, assuming that Sm fluctuations of $\sigma_{Sm} = 0.25$ Å in YbB_6 and at most $\sigma_{Sm} = 0.15$ Å in LaB_6.

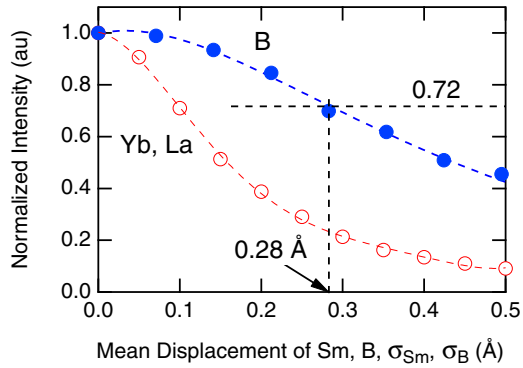

FIG. 9. Normalized intensity of the atomic images as a function of positional fluctuation of Sm and B. The open circles indicate the intensity of the first-NN Yb or La with Sm fluctuation σ_{Sm}. For the calculation, Yb and La are fixed at the ideal positions. The closed circles indicate the intensity of the first-NN B with Sm fluctuation $\sigma_{Sm} = 0.25$ Å. The dashed curves are results of the fitting using a fifth polynomial curve.

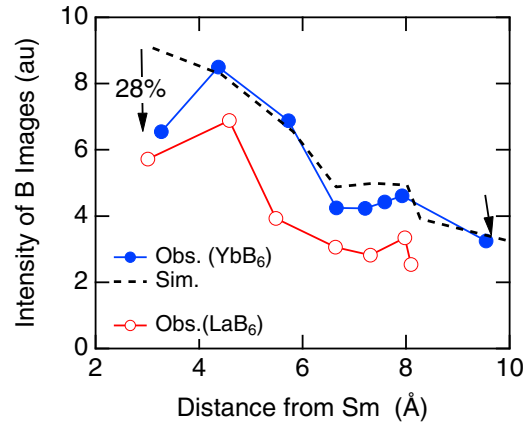

FIG. 10. Intensity of B images around Sm of Sm-doped RB_6 (R = Yb, La). The horizontal axis is distance from Sm. The dashed line indicates the simulation using a model of nondoped RB_6 structure.

From the isotropic atomic displacement parameters determined by diffraction experiments, the mean-square displacement $\sqrt{\langle u^2 \rangle}$ of Yb and La in nondoped RB_6 is estimated as 0.1017(2) Å [13,14]. Comparing with these values, the fluctuation of Sm, $\sigma_{Sm} = 0.25(4)$ Å in YbB_6 is 2.5 times larger than $\sqrt{\langle u^2 \rangle}$, meaning that the fluctuation of Sm atoms cannot be explained just by the thermal vibration of the RB_6 lattice.

First-principles calculations have shown that the coupling between rare-earth ions in $R^{2+}B_6$ is stronger than that in $R^{3+}B_6$ [9]. This implies that the coupling between Sm^{3+} and Yb^{2+} ions is weaker than that between Yb^{2+} ions; consequently, Sm^{3+} is relatively easier to move in the boron cage than Yb^{2+}. Moreover, as mentioned above, the difference of the lattice constants of LaB_6 and YbB_6 (∼0.01 Å) is 20 times smaller than the difference of the ionic radius of Sm^{2+} and Sm^{3+} (∼0.2 Å), indicating that the free space in the boron cage for fluctuation of Sm^{3+} in YbB_6 is much larger than that of Sm^{2+} in LaB_6. These must be the reasons that the Sm atoms in YbB_6 have larger fluctuations than those in LaB_6.

C. Doping effect to the boron cage

Next, we discuss the effects of doping on the boron cage itself. Although we examined the behavior of the Sm atoms based on the widths of the profiles, it is difficult to estimate the σ of B atoms quantitatively because of contamination of many artifacts as shown in Fig. 6, and the weak intensity of B atomic images as compared with R in Fig. 5, in particular for LaB_6. Thus, we will discuss the behavior of B based on the intensities of its atomic images. Figure 10 shows the distance dependence of the intensity of the atomic images of B in Sm-doped RB_6 (R = Yb and La) along the radial direction. The intensity of B in Sm-doped YbB_6 is well represented by the simulation (dashed line) except for the first-NN B, where the intensity of the observed atomic image is suppressed. This implies that the first-NN B is fluctuating due to the Sm doping, while the second NN and the further B atoms show no obvious fluctuations. Similar suppressions of the first-NN B were observed in Sm-doped LaB_6, as well. The suppression of the intensity of the first-NN B in Sm-doped YbB_6 is 28%.

To estimate the fluctuations of the first-NN B, σ_B, we calculated the effect of the fluctuations of B on the intensity. The fluctuation of the first-NN B around the ideal position is calculated by the same way mentioned previously using the Box-Muller method. In the calculations, the mean displacement of Sm, σ_{Sm}, is fixed to be 0.25 Å, which was estimated from the profile in Fig. 7. The intensity of the B atomic images is shown in Fig. 9, which monotonically decreases with increasing mean displacement of B, σ_B. The horizontal dashed line shows the obtained intensity of the first-NN B in Fig 10, indicating that the first-NN B fluctuates with $\sigma_B = 0.28$ Å. Using the reported displacement parameters of B in nondoped YbB_6 determined by diffraction experiments, the mean displacement $\sqrt{\langle u^2 \rangle}$ of B by thermal vibration is estimated as 0.068(3) Å [13]. Since the fluctuation of the first-NN B ($\sigma_B = 0.28$ Å) cannot be interpreted just by the thermal vibration in nondoped RB_6, and the intensity of only the first-NN B is suppressed, then the fluctuation of B must be caused by Sm doping.

As mentioned above, the fluctuations of R(Yb, La) and B (except the first-NN B around the Sm dopants) are not observed in the present measurements, while the first-NN B is fluctuating due to the Sm doping. Therefore, the effect of the doping on the lattice is limited to the outer region of the first-NN boron cage because of the strong covalent bond in the boron-cage network. Ying *et al.* found that the Yb-B bond in YbB_6 is more compressible than the B-B bond under ambient pressure by extended x-ray absorption fine-structure spectroscopy under high pressures [11]. When Yb is replaced by Sm, the Sm can be moved in the boron cage because of the relatively soft bonding of Sm-B, assuming that the bonding of Sm-B and Yb-B are the same, while the bonding in the boron cage is rigid, which suppresses the fluctuations of B in

the boron-cage network, with the exception of the cage of the first-NN B.

On the other hand, the intensity of the second NN and the more distant B in RB_6 (R = Yb, La) in Fig. 10 is not consistent with the scattering length b. Basically, since the intensity of the atomic images is proportional to b of the atoms [39,40], the intensities of B in LaB_6 and YbB_6 in Fig. 10 have to be the same, when all the fluctuation is negligible. As discussed above, the fluctuations of Sm in YbB_6 and LaB_6 are estimated as $\sigma_{Sm} = 0.25$ Å in YbB_6 and $\sigma_{Sm} = 0.15$ Å in LaB_6, respectively. Since these fluctuations reduce the intensity of the B atomic images, the intensity of B in LaB_6 is expected to be 1.5 times the intensity of B in YbB_6 based on the same estimation of the fluctuation of Sm in LaB_6, when the fluctuation of B is the same in both samples. However, the intensity of B in LaB_6 in Fig. 10 is only roughly 0.7 times of that in YbB_6, suggesting that the intensity of B in LaB_6 is further reduced by approximately 0.5 times by some other effect.

A possible model to explain the suppression of $\sim\frac{1}{2}$ of the intensity of the B atomic images is the on-phase vibration of Sm and B in LaB_6. The hologram of Sm-doped LaB_6 in Fig. 4 is less visible in comparison with that of Sm-doped YbB_6, suggesting that it is probable that the fluctuations or vibrations of atoms in Sm-doped LaB_6 are different from those in Sm-doped YbB_6. In the atomic reconstruction in Fig. 11(a) which is the central part of Fig. 6(b), in which the B atomic images are emphasized for discussion, the B atomic images in LaB_6 deviate from the expected positions of the nondistorted RB_6 along the [100] directions. This suggests that either B *or* Sm deviates from the expected position. However, if B is simply deviated from the expected position along the [100] directions, the suppression of the atomic image intensity cannot be explained. A possible scenario is that there exist potential minima of Sm and La around the center of the boron cage in Sm-doped LaB_6, and Sm is located at one of these minimum potential positions. In Fig. 11(b), an image of the potential minimum of Sm of this model is shown. As discussed above, the peak profile of La is sharper than that of Yb and B in YbB_6: $\sigma_{Sm} = 0.25(4)$ Å in YbB_6 and $\sigma_{Sm} = 0.15$ Å in LaB_6. From a vibration point of view, this implies a model wherein Sm and La in the vicinity of Sm in Sm-doped LaB_6 are vibrating with the same phase in the potential minimum as shown in Fig. 11. In this situation, the B positions on the reconstructed images deviate along the [100] directions, while the La position is the same as that of the nondoped RB_6 when La is located in the same potential minimum as that of Sm. If B_1 is vibrating with the same phase as Sm, the broadening of the atomic images is relatively reduced, while if B_2 is vibrating with off phase owing to the mirror symmetry, the atomic images become broader. This broadening also causes the suppression of the intensity of off-phase B_2, which makes the atomic images of off-phase B_2 less visible, while on-phase B_1 can be observed with sharper width. Moreover, since B_3 has the same phase with B_1, a sharp B image of B_3 is also observed. The sharpness of the atomic images of B_1 and B_3 in Sm-doped LaB_6 supports this on-phase vibration model. In this model, six potential minima are expected around the center of the boron cage. Thus, the B image splits into six images and only B with

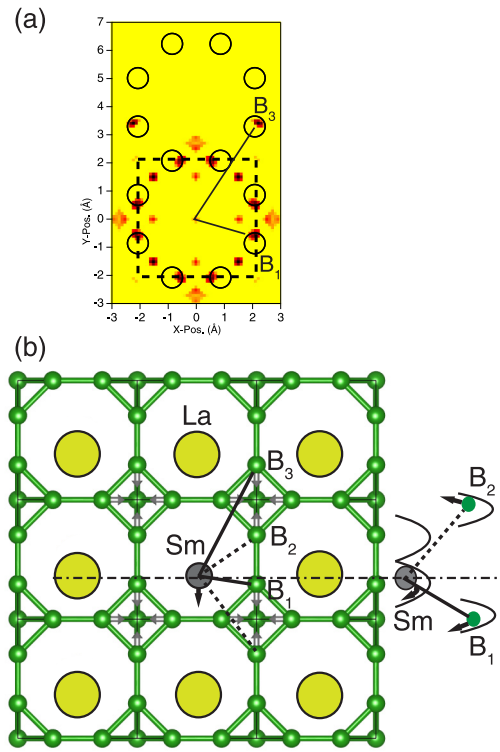

FIG. 11. (a) The central part of Fig. 6(b) and (b) a possible model of on-phase vibrations in LaB_6. Sm (small gray circle) and La are vibrating around a potential minimum. The horizontal chain line indicates the averaged positions of Sm and La. The black arrow at Sm and gray arrows at B indicate direction of vibrations of La and B at a moment. The B_1 is vibrating with same phase with Sm and La, while B_2 has off-phase vibrations. The solid and dashed lines indicate relations of on and off phase between Sm and B.

on-phase vibration can be observed, which makes the intensity of observed B roughly $\frac{1}{6}$ of the expected intensity.

Assuming that the relative fluctuation between Sm and B (excluding the first-NN B) in this on-phase model can be neglected in comparison with the $\sigma_{Sm} = 0.15$ Å by fluctuation between Sm and La in LaB_6, the reduction of the intensity of B in LaB_6 caused by the fluctuation of B is negligible. On the other hand, since the B atomic images in YbB_6 in Fig. 6(b) are obviously broader than those in LaB_6, the relative fluctuation between Sm and B in YbB_6 is larger than that in LaB_6. If the relative fluctuation of $\sim$0.2 Å between B and Sm in YbB_6 can be assumed, the intensity of B in YbB_6 becomes $\sim\frac{1}{3}$ of that without the relative fluctuation. Consequently, the intensity ratio of B between LaB_6 and YbB_6 in this on-phase model becomes $\sim\frac{1}{2}$, which is consistent with the observed suppression in Fig. 10. Thus, the suppression of the B atomic image intensity in LaB_6 in Fig. 10 can be understood as the difference of relative fluctuations between Sm and B. This on-phase model with double potential minima is a local behavior which is realized only around Sm. However, such double potential behavior may be similar with the rattling motions in the cage-type structure, for instance, the rattling motions of Pr in the filled skutterudite $PrOs_4Sb_{12}$, in which characteristic vibrations with double potentials are observed [54]. The consistency of the intensity of B by the on-phase

model implies that Sm doping may cause similar double potential minima locally around the Sm dopants.

IV. CONCLUSION

We performed the newly developed MNH for 2% Sm-doped RB_6 (R = Yb, La). We have succeeded in visualizing the local atomic images around Sm, and found the effects of the doping on the lattice. We found that the fluctuations of Sm in YbB_6 are more obvious than those of Sm in LaB_6 because of the difference of space for rare-earth motions in the boron cage, which is similar to the trend observed by Raman spectroscopy and inelastic x-ray scattering. The first-NN B also shows fluctuation caused by the Sm doping, while the effects on Yb, La, and the more distant B are not observable, meaning that the effects of doping on lattice are limited to the outer region of the first-NN boron cage. These are the first observations of the local behavior of doped rare-earth atoms and B in rare-earth borides with boron cages. These results suggest that MNH is essential for the microscopic investigations of the effects of doping on lattices, in particular, to light elements.

ACKNOWLEDGMENTS

The authors would like to thank T. Yamamoto, and K. Sugimoto of Ibaraki University for their support to multiple-wavelength neutron holography experiments. This work is partly supported by the Grant-in-Aid for Exploratory Research (Grant No. 24656004), Grant-in-Aid for Scientific Research (A) (Grant No. 19H00655) and (C) (Grant No. 17K05116), and Grant-in-Aid for Scientific Research on Innovative Areas (Grants No. 26105001, No. 26105006, and No. 19H05045) from the Ministry of Education, Culture, Sports, Science, and Technology of Japan. The neutron experiments were performed under the user program of the Materials and Life Science Experimental Facility of the J-PARC (Proposals No. 2017A0124, No. 2017A0108, No. 2017B0166, and No. 2018B0049).

[1] J. T. Cahill and O. A. Graeve, J. Mater. Res. Technol. **8**, 6321 (2019).
[2] T. Mori, in *Handbook on the Physics and Chemistry of Rare Earths*, edited by J. K. A. Gschneidner, J.-C. Bunzli, and V. Pecharsky, Vol. 38 (North-Holland, Amsterdam, 2008), p. 105.
[3] K. Iwasa, R. Igarashi, K. Saito, C. Laulhé, T. Orihara, S. Kunii, K. Kuwahara, H. Nakao, Y. Murakami, F. Iga, M. Sera, S. Tsutsui, H. Uchiyama, and A. Q. R. Baron, Phys. Rev. B **84**, 214308 (2011).
[4] K. Iwasa, K. Kuwahara, Y. Utsumi, K. Saito, H. Kobayashi, T. S. and M. Amano, T. Hasegawa, N. Ogita, M. Udagawa, S. Tsutsui, and A. Q. R. Baron, J. Phys. Soc. Jpn. **81**, 113601 (2012).
[5] K. Iwasa, F. Iga, A. Yonemoto, Y. Otomo, S. Tsutsui, and A. Q. R. Baron, J. Phys. Soc. Jpn. **83**, 094604 (2014).
[6] D. A. Serebrennikov, E. S. Clementyev, and P. A. Alekseev, J. Exp. Theor. Phys. **123**, 452 (2016).
[7] N. Ogita, T. Hasegawa, M. Udagawa, F. Iga, and S. Kunii, J. Phys.: Conf. Ser. **176**, 012032 (2009).
[8] N. Ogita, S. Nagai, N. Okamoto, M. Udagawa, F. Iga, M. Sera, J. Akimitsu, and S. Kunii, Phys. Rev. B **68**, 224305 (2003).
[9] M. Udagawa, T. Hasegawa, Y. Takasu, N. Ogita, K. Suekuni, and M. A. Avila, J. Phys. Soc. Jpn. **77**, 142 (2008).
[10] J. M. Trascon, Y. Ishikawa, B. Chevalier, J. Etourneau, P. Hagenmuller, and M. Kasaya, J. Phys. (Paris) **41**, 1135 (1980).
[11] J. Ying, L. Tang, F. Chen, X. Chen, and V. V. Struzhkin, Phys. Rev. B **97**, 121101(R) (2018).
[12] R. D. Shannon, Acta Crystallogr. A. **32**, 751 (1976).
[13] M. Blomberg, M. Merisalo, M. Korsukov, and V. Gurin, J. Alloys Compd. **217**, 123 (1995).
[14] Y. Takahashi, K. Ohshima, F. Okamura, A. Otani, and T. Tanaka, J. Phys. Soc. Jpn. **68**, 2304 (1999).
[15] A. Szöke in *Short Wavelength Coherent Radiation: Generation and Applications*, edited by D. T. Attwood and J. Boker, AIP Conf. Proc. No. 147 (American Institute of Physics, New York, 1986).
[16] G. R. Harp, D. K. Saldin, and B. P. Tonner, Phys. Rev. B **42**, 9199 (1990).
[17] M. Tegze and G. Faigel, Nature (London) **380**, 49 (1996).
[18] K. Hayashi, N. Happo, S. Hosokawa, W. Hu, and T. Matsushita, J. Phys.: Condens. Matter **24**, 093201 (2012).
[19] K. Hayashi and P. Korecki, J. Phys. Soc. Jpn. **87**, 061003 (2018).
[20] W. Hu, K. Hayashi, T. Fukumura, K. Akagi, M. Tsukada, N. Happo, S. Hosokawa, K. Ohwada, M. Takahasi, M. Suzuki, and M. Kawasaki, Appl. Phys. Lett. **106**, 222403 (2015).
[21] W. Hu, K. Hayashi, K. Ohwada, J. Chen, N. Happo, S. Hosokawa, M. Takahasi, A. A. Bokov, and Z. G. Ye, Phys. Rev. B **89**, 140103(R) (2014).
[22] K. Hayashi, N. Uchitomi, K. Yamagami, A. Suzuki, H. Yoshizawa, J. T. Asubar, N. Happo, and S. Hosokawa, J. Appl. Phys. **119**, 125703 (2016).
[23] Y. Wakabayashi, D. Nakajima, Y. Ishiguro, K. Kimura, T. Kimura, S. Tsutsui, A. Q. R. Baron, K. Hayashi, N. Happo, S. Hosokawa, K. Ohwada, and S. Nakatsuji, Phys. Rev. B **93**, 245117 (2016).
[24] A. Sato-Tomita, N. Shibayama, N. Happo, K. Kimura, T. Okabe, T. Matsushita, S.-Y. Park, Y. C. Sasaki, and K. Hayashi, Rev. Sci. Instrum. **87**, 063707 (2016).
[25] T. Yamamoto, K. Hayashi, N. Happo, S. Hosokawa, and H. Tajiri, Acta Mater. **131**, 534 (2017).
[26] S. Hosokawa, J. R. Stellhorn, T. Matsushita, N. Happo, K. Kimura, K. Hayashi, Y. Ebisu, T. Ozaki, H. Ikemoto, H. Setoyama, T. Okajima, Y. Yoda, H. Ishii, Y. F. Liao, M. Kitaura, and M. Sasaki, Phys. Rev. B **96**, 214207 (2017).
[27] T. He, X. Yang, T. Terao, T. Uchiyama, T. Ueno, K. Kobayashi, J. Akimitsu, T. Miyazaki, T. Nishioka, K. Kimura, K. Hayashi, N. Happo, H. Yamaoka, H. Ishii, Y. F. Liao, H. Ota, H. Goto, and Y. Kubozono, Phys. Rev. B **97**, 104503 (2018).
[28] K. Tsutsui, T. Matsushita, K. Natori, T. Muro, Y. Morikawa, T. Hoshii, K. Kakushima, H. Wakabayashi, K. Hayashi, F. Matsui, and T. Kinoshita, Nano Lett. **17**, 7533 (2017).
[29] T. D. Beynon and A. G. Pink, Nature (London) **283**, 749 (1980).

[30] D. Sarenac, M. G. Huber, B. Heacock, M. Arif, C. W. Clark, D. G. Cory, C. B. Shahi, and D. A. Pushin, Opt. Express **24**, 22528 (2016).
[31] L. Cser, G. Krexner, and G. Török, Europhys. Lett. **54**, 747 (2001).
[32] B. Sur, R. B. Rogge, R. P. Hammond, V. N. P. Anghel, and J. Katsaras, Nature (London) **414**, 525 (2001).
[33] L. Cser, G. Török, G. Krexner, I. Sharkov, and B. Faragó, Appl. Phys. Lett. **85**, 1149 (2004).
[34] L. Cser, G. Török, G. Krexner, I. Sharkov, and B. Faragó, Phys. Rev. Lett. **89**, 175504 (2002).
[35] L. Cser, B. Farago, G. Krexner, M. Markó, I. Sharkov, and G. Török, Phys. Rev. Lett. **97**, 255501 (2006).
[36] K. Hayashi, K. Ohoyama, S. Orimoa, Y. Nakamori, H. Takahashi, and K. Shibata, Jpn. J. Appl. Phys. **47**, 2291 (2008).
[37] K. Hayashi, K. Ohoyama, S. I. Orimo, H. Takahashi, and K. Shibata, Phys. Rev. B **91**, 024102 (2015).
[38] A. Szakál, M. Markó, and L. Cser, Phys. Rev. B **93**, 174115 (2016).
[39] K. Ohoyama and K. Hayashi, Phys. Status. Solidi B **255**, 1800143 (2018).
[40] K. Hayashi, K. Ohoyama, N. Happo, T. Matsushita, S. Hosokawa, M. Harada, Y. Inamura, H. Nitani, T. Shishido, and K. Yubuta, Sci. Adv. **3**, e1700294 (2017).
[41] K. Oikawa, F. Maekawa, M. Harada, T. Kai, S. Meigo, Y. Kasugai, M. Ooi, K. Sakai, M. Teshigawara, S. Hasegawa, M. Futakawa, and Y. Ikeda, Nucl. Instrum. Methods Phys. Res., Sect. A **589**, 310 (2008).
[42] F. Maekawa, M. Harada, K. Oikawa, M. Teshigawara, T. Kai, S. Meigo, M. Ooi, S. Sakamoto, H. Takada, M. Futakawa, T. Kato, Y. Ikeda, N. Watanabe, T. Kamiyama, S. Torii, R. Kajimoto, and M. Nakamura, Nucl. Instrum. Methods Phys. Res., Sect. A **620**, 159 (2010).
[43] C. Yonezawa, M. Magara, H. Sawahata, M. Hoshi, Y. Ito, and E. Tachikawa, J. Radioanal. Nucl. Chem. **193**, 171 (1995) in Japanese.
[44] F. Iga, N. Shimizu, and T. Takabatake, J. Magn. Magn. Mater. **177-181**, 337 (1989).
[45] A. Rauch and W. Waschkowski, in *Neutron Data Booklet*, edited by A.-J. Dianoux and G. Lander (Institut Laue Langevin, Grenoble, 2002), pp. 1.1-8–1.1-19.
[46] Y. Inamura, T. Nakatani, J. Suzuki, and T. Otomo, J. Phys. Soc. Jpn. **82**, SA031 (2013).
[47] B. Zhang, J. Yang, L. Jin, C. Ye, J. Bashir, N. M. Butt, M. Siddique, M. Arshed, and Q. H. Khan, Acta Crystallogr. **A46**, 435 (1990).
[48] J. J. Barton, Phys. Rev. Lett. **61**, 1356 (1988).
[49] J. J. Barton, Phys. Rev. Lett. **67**, 3106 (1991).
[50] N. Happo, T. Hada, A. Kubota, Y. Ebisu, S. Hosokawa, K. Kimura, H. Tajiri, T. Matsushita, and K. Hayashi, Jpn. J. Appl. Phys. **57**, 058006 (2018).
[51] N. Happo, K. Hayashi, and S. Hosokawa, Jpn. J. Appl. Phys. **49**, 116601 (2010).
[52] W. Hu, K. Hayashi, T. Yamamoto, N. Happo, S. Hosokawa, T. Terai, T. Fukuda, T. Kakeshita, H. Xie, T. Xiao, and M. Suzuki, Phys. Rev. B **80**, 060202(R) (2009).
[53] S. Hosokawa, N. Happo, and K. Hayashi, Phys. Rev. B **80**, 134123 (2009).
[54] K. Kaneko, N. Metoki, H. Kimura, Y. Noda, T. D. Matsuda, and M. Kohgi, J. Phys. Soc. Jpn. **78**, 074710 (2009).